MIT Libraries | DSpace@MIT

MIT Open Access Articles

Correlating stress generation and sheet resistance in InAlN/GaN nanoribbon high electron mobility transistors

Massachusetts Institute of Technology

Correlating stress generation and sheet resistance in InAlN/GaN nanoribbon high electron mobility transistors

Eric J. Jones, Mohamed Azize, Matthew J. Smith, Tomás Palacios, and Silvija Gradečak

Additional information on Appl. Phys. Lett.

Correlating stress generation and sheet resistance in InAlN/GaN nanoribbon high electron mobility transistors

Eric J. Jones,[1] Mohamed Azize,[2] Matthew J. Smith,[1] Tomás Palacios,[2] and Silvija Gradečak[1]

[1]*Department of Materials Science and Engineering, Massachusetts Institute of Technology, Cambridge, Massachusetts 02139, USA*

[2]*Department of Electrical Engineering and Computer Science, Massachusetts Institute of Technology, Cambridge, Massachusetts 02139, USA*

We report the nanoscale characterization of the mechanical stress in InAlN/GaN nanoribbon-structured high electron mobility transistors (HEMTs) through the combined use of convergent beam electron diffraction (CBED) and elastic mechanical modeling. The splitting of higher order Laue zone lines in CBED patterns obtained along the [540] zone axis indicates the existence of a large strain gradient in the *c*-direction in both the planar and nanoribbon samples. Finite element models were used to confirm these observations and show that a passivating layer of Al_2O_3 can induce a tensile stress in the active HEMT layer whose magnitude is dependent on the oxide layer thickness, thus, providing important ramifications for device design and fabrication. © *2012 American Institute of Physics*. [http://dx.doi.org/10.1063/1.4752160]

Due to their inherently one-dimensional structure and high surface-to-volume ratio, nanowires and nanoribbons offer promising routes toward integration of III/V materials on silicon[1] and realization of heterostructures not achievable by thin film techniques.[2–4] The ability of nanostructured materials to efficiently relax stress at heterointerfaces is especially important for the realization of advanced electronic and optical devices and can be used to further tune device properties such as emission wavelengths[2,5] or electronic carrier characteristics such as mobility.[4,6] At the same time, characterization of stress and strain in these nanostructures is inherently difficult; techniques typically used in bulk systems—such as x-ray diffraction and micro-Raman spectroscopy—lack the spatial resolution needed to probe stress on the nanoscale. Convergent beam electron diffraction (CBED) is a technique that can be used to measure strains as low as 10^{-4} and with spatial resolutions on the order of 1 nm, making it a powerful tool for stress/strain state characterization of nanostructured devices. This level of precision is achieved by tracking higher order Laue zone (HOLZ) lines resulting from the diffraction of electrons off high order lattice planes, which makes their position highly sensitive to changes in lattice parameters caused by strain. Traditionally, CBED has only been useful for characterizing regions of samples containing small homogenous strain fields[7] due to the complex splitting of HOLZ line patterns that are produced from a strain gradient.[8] However, recent work has shown that a combination of kinematic diffraction simulations and elastic mechanical modeling can be a powerful approach in determining the stress state of highly strained samples.[9]

Due to its wide bandgap and high electron mobility, GaN is an important materials system for the realization of high-frequency and high-power electronic device applications. Traditionally, an AlGaN barrier has been used for the fabrication of GaN-based high electron mobility transistor (HEMT) devices; however, due to the large lattice mismatch at the AlGaN/GaN interface, the performance and reliability of these devices is often limited by strain induced defects[10] or strain relaxation.[11] It has therefore been proposed that InAlN could be used as an alternative to AlGaN due to its ability to be grown lattice-matched on GaN while maintaining a high intrinsic polarization difference with GaN, necessary for a high charge density in the channel.[12] It has also been shown that the carrier concentration in an InAlN/GaN heterojuction can be enhanced through the application of a tensile stress[13] making it a promising candidate for piezo-doping. Recently, nanoribbon structures were purposed as a promising route towards mitigating device performance degradation due to scaling effects through further confinement of electronic carriers.[14,15] In studying nanoribbon-structured InAlN/GaN HEMT devices, it was shown that the sheet resistivity of the devices decreased as the thickness of the passivating Al_2O_3 layer increased, and that significant improvement could be achieved over planar-structured devices when the thickness of the Al_2O_3 layer was sufficient to cause a planarization of the oxide layer. The significant decrease in sheet resistance was attributed to an additional tensile stress introduced by the passivating oxide layer, which could increase the electronic carrier concentration at the InAlN/GaN interface thereby lowering sheet resistance, although the exact mechanism has remained unknown. Therefore, to further enhance device fabrication and performance, understanding the stress generation mechanisms is critical for future tailoring of HEMT device performance. In this work, we use CBED combined with finite element analysis (FEA) to measure the evolution of stress in nanoribbon-structured InAlN/GaN HEMTs. These results are then used to explain trends in sheet resistance that were observed as a function of passivating oxide thickness.[15]

Nanoribbon HEMT structures were fabricated through a previously published top-down process.[15] InAlN/GaN layers were grown on a SiC substrate using metal-organic chemical vapor deposition. The HEMT structure consists of a

~1.8 μm thick Fe-doped GaN layer grown on SiC, followed by the deposition of a ~1 nm AlN barrier layer, and finally a ~7 nm layer of $In_{0.17}Al_{0.83}N$ (nominal composition). Transmission electron microscopy (TEM) investigations were performed on as-grown layers that were subjected to standard device fabrication steps. The process begins with mesa isolation performed using electron cyclotron resonance reactive ion etching (ECR-RIE). Ti/Al/Ni/Au metal stacks were then deposited and annealed to form ohmic source and drain contacts. Nanoribbons were next defined between the ohmic contacts of a number of devices using electron beam lithography and fabricated using low-power ECR-RIE, while other devices retained their planar structure for comparison. A conformal layer of Al_2O_3 was deposited on the surface of all samples using atomic layer deposition (ALD) with various thicknesses ranging from 0–45 nm. TEM samples were obtained from the region between the source and drain contacts using focused ion beam (FIB). A 2 μm thick Pt layer was deposited during FIB preparation to protect the HEMT layers from the damaging effects of the Ga beam during course milling at 30 kV. Final thinning of the sample was performed at 5 kV to ensure a high quality surface for TEM. TEM investigations were performed using a JEOL 2010F equipped with a field-emission electron source and operated at an accelerating voltage of 200 kV. CBED patterns were obtained using spot size of approximately 1 nm and a convergence angle of 30 mrad. All diffraction simulations were performed using the JEMS software suite.[16]

We first employed CBED to measure local changes in stress state of the electron-transparent TEM samples fabricated from both planar and nanoribbon HEMT devices. Cross-sectional dark-field scanning TEM (DF-STEM) images of representative planar and nanoribbon structures (Figs. 1(a) and 1(b), respectively) show the device structure consisting of the GaN substrate, InAlN HEMT layer, and 45 nm passivating Al_2O_3; we note that 1 nm AlN barrier layer is not visible at this magnification. We measured the strain state of both planar and nanoribbon HEMT structures by recording CBED patterns in these samples at different distances from the InAlN/Al_2O_3 interface, as discussed below. The strain state of a thin TEM sample can be determined by analyzing both the position and width of individual HOLZ lines contained in the CBED pattern;[17] a non-uniform strain field—like the one created due to free surface relaxation—will cause HOLZ lines to broaden and split forming HOLZ bands whose width is directly related to the sample strain gradient along the direction of the electron beam.[8] The characterization of strain is best achieved using off-axis CBED patterns due to the dynamic diffraction effects that result from the interaction of various diffracted beams within the sample and are prominent along high-symmetry zone axes. Dynamic effects can be minimized by tilting the sample to a low-symmetry axis where fewer beams meet the appropriate diffraction criteria and produce a pattern that contains a high number of sharp, well-defined HOLZ lines. In this study, the [540] zone axis was found experimentally as the most appropriate for CBED studies and was indexed using kinematic simulations. Dynamic simulations were performed to confirm the lack of significant dynamic diffraction effects and were also used to
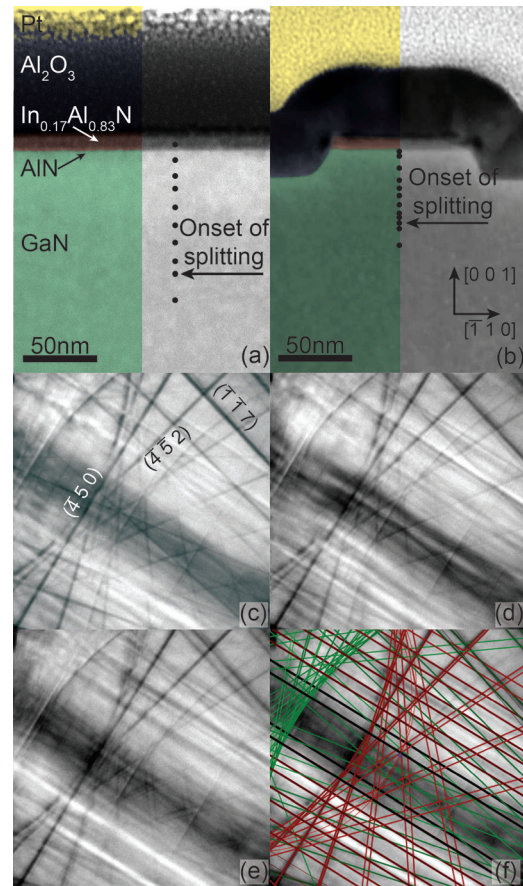

FIG. 1. DF-STEM images of representative (a) planar and (b) nanoribbon HEMT structures showing relative positions in each sample where CBED patterns were collected (indicated as dots in each image). Arrows indicate onset of HOLZ line splitting. (c)-(f) A series of CBED patterns collected from the planar HEMT structure a distance of (c) 113.3 nm, (d) 74.7 nm, and (e) 51.0 nm beneath the Al_2O_3/InAlN interface. In (f), two sets of kinematic simulations—shown as red and green lines—are used to approximate the splitting observed in the CBED pattern from (e).

determine sample thickness with accuracy of approximately ±5 nm.

Series of CBED patterns were obtained from both samples in a line perpendicular to the InAlN/AlN/GaN HEMT interface beginning in the bulk and moving closer to the InAlN/Al_2O_3 interface [Figs. 1(c)–1(g)]. Far away from the interface (>100 nm), CBED patterns are observed to have well-defined, sharp HOLZ lines indicating a relaxed, strain-free region of the sample [Fig. 1(c)]. Patterns from these regions were used to determine the thickness of each sample to be 70 nm and 90 nm for the nanoribbon and planar samples, respectively. Moving closer to the HEMT interface, HOLZ lines begin to split and broaden. Moreover, by examining the series of patterns from both the planar and nanoribbon samples, we observed that HOLZ lines that are highly indexed in the c-direction, such as the $(1\bar{1}\,\bar{7})$, begin to split further away from the interface than the lines with low c indices, such as the $(\bar{4}50)$. This finding indicates the existence of a significant strain gradient in the [001] direction. Comparing CBED patterns from the two samples, it can be observed that splitting begins further away from the HEMT interface in the planar sample compared to the nanoribbon sample, as indicated by the arrows in Figs. 1(a) and 1(b);

however, the origin of this difference cannot be fully understood from these patterns alone.

To quantify and compare the HOLZ line splitting observed in each sample, kinematic simulations were used to approximate the width of each HOLZ band. If the surface of the deformed lattice is assumed to be fully relaxed but tilted away from its original orientation by some angle $\theta/2$, diffraction from the sample then can be approximated as occurring from two pieces of strain-free material—the front and back surfaces—tilted with respect to one another about the [-110] direction as indicated in Figure 1 by a total angle of θ.[9] Experimental patterns obtained far away from the HEMT interface were first matched to kinematic simulations to determine experimental parameters such as effective accelerating voltage, angle of convergence, etc. Using these parameters, two simulated sets of HOLZ lines were then superimposed upon one another to approximate the splitting observed in the experimental images, as illustrated in Fig. 1(h). The shift in the HOLZ line patterns corresponds to the angle of rotation θ between the two surfaces of the sample and gives an indication of the level of strain relaxation. This method was used to generate splitting profiles for both the planar and nanoribbon samples [Fig. 2(c)]. While the overall trends appear similar in both planar and nanoribbon samples indicating that the source stress in both systems is the same, the magnitude of splitting in these two samples is different.

To understand these differences, we created 3D finite element models of the planar and nanoribbon TEM structures and calculated the stresses and strains resulting from the inherent lattice mismatch of each device layer. Fig. 2(a) shows a schematic of the model consisting of a $2\,\mu m$ fully relaxed GaN substrate, 1 nm AlN barrier layer, and 8 nm $In_{0.17}Al_{0.83}N$ and 45 nm of Al_2O_3 corresponding to the samples used for CBED investigation. Orthotropic elastic constants used for the modeling were obtained from the experimental work summarized by Wright[18] and Vegard's rule of mixing was used to determine the elastic constants of the InAlN layer based on an In composition of 0.17 at. %. Similar to other studies,[19] the lattice mismatch between each layer was modeled as a thermal expansion of each material with GaN as a reference and the stress in the system was assumed to be fully compensated elastically. Dimensions of each model were based upon those observed in TEM with the thickness obtained from dynamic CBED simulations.

To compare the FEA model with experimental results, band plots of the strain components ε_{xx}, ε_{yy}, and ε_{zz} were generated along the direction of the electron beam through the sample [Figure 2(b)]. These plots reveal the spatial distribution and magnitude of all three strain components and show that the variation of the ε_{zz} strain component is considerably higher than either the ε_{xx} or ε_{yy} components. Line scans of the strain components at 60 nm and 30 nm below the Al_2O_3/InAlN interface [Fig. 2(c) inset] show that the total variation of ε_{zz} increases from 2.6×10^{-4} at 60 nm to 5.6×10^{-4} at 30 nm, which is 2–5 times greater than the variations observed for ε_{xx} (9.6×10^{-5}–1.2×10^{-4}) and an order of magnitude greater than those for ε_{yy} (1.0×10^{-5}–5.7×10^{-5}). The strong variation of the ε_{zz} strain component corroborates the CBED results and the observation that HOLZ lines highly indexed in the c-direction exhibit stronger splitting behavior. Splitting profiles were obtained by measuring the angle of the model's deformed surface with respect to its original orientation and are shown together with the experimentally measured splitting in Fig. 2(c). The FEA model correctly replicates the overall splitting behavior, but it consistently underestimates the magnitude of splitting observed experimentally. We suggest that this difference in magnitude could indicate a stress generated during the processing of the device structure that is not represented in the FEA model. The model also highlights the importance of sample thickness showing that the difference between the planar (90 nm thick) and nanoribbon (70 nm thick) splitting profiles is due to the difference in sample thickness. This observation was also confirmed experimentally by obtaining splitting profiles from nanoribbon structures of differing thicknesses along a wedge shaped sample in which stronger splitting behavior was observed to occur in thicker regions of the sample.

Finally, using this FEA model, full device structures (as opposed to thin-film TEM foils described above) were modeled to investigate the role of nanoribbon fabrication and Al_2O_3 passivation on the stress state of the HEMT structure both along (σ_{xx}) and perpendicular (σ_{yy}) to the ribbon direction. It was observed from the model of the nanoribbon device that the largest variations in stress occurred along the σ_{yy} component, due to the fact that the greatest amount of stress relaxation will occur perpendicular to the newly created sidewall facets of the nanoribbon structure. The average σ_{yy} stress in the InAlN layer for both planar and nanoribbon
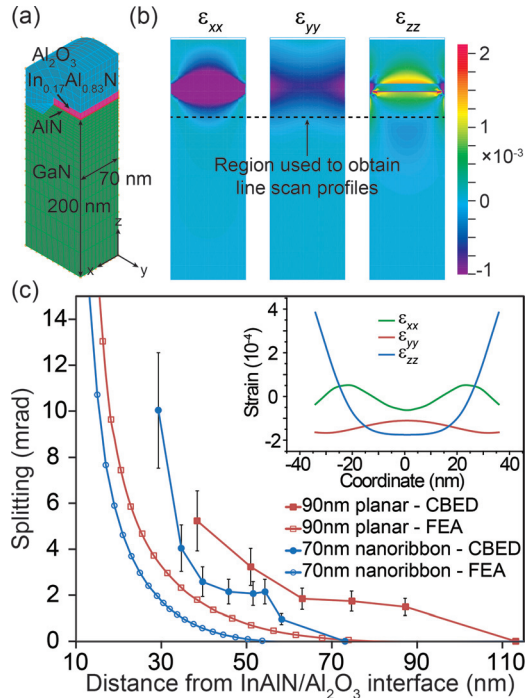

FIG. 2. (a) Schematic of FEA model developed to analyze HOLZ line splitting due to lattice mismatch. (b) Band plots comparing the strain gradients of the ε_{xx}, ε_{yy}, and ε_{zz} components through the thickness of a TEM sample generated using FEA. Comparing the three plots on the same scale reveals the large gradient of ε_{zz} compared to the other directions. Line scans of each strain component were obtained along a line approximately 30 nm below the AlN/GaN interface (dashed line) and are shown in the inset of (c). (c) Splitting profiles obtained from the experimental CBED patterns using a free surface total relaxation assumption and compared to profiles generated from FEA modeling—all lines are used as guides to the eye.

structures is shown as a function of Al_2O_3 thickness in Fig. 3. From these plots, it can be seen that the creation of a nano-ribbon in a planar structure results in a compressive stress of approximately 10 MPa. The application of an oxide layer releases this compressive stress and introduces a tensile stress that increases up to 420 MPa as the thickness of the oxide covering the HEMT layers increases. The σ_{xx} component (not shown) exhibits a similar trend though the stress remains tensile and the total change in magnitude is smaller, varying only from 460 MPa with no passivating oxide layer to 623 MPa for a 45 nm thick layer. In contrast to the nano-ribbon structures, the predicted stress, σ_{yy}, of the planar device is on the order of 745 MPa and only increases slightly with oxide thickness in a linear fashion [Fig. 3]. The compressive strain that is observed in the unpassivated nanorib-bon is the result of a new free surface that allows for relaxation of the biaxial tensile stress that is generated in the thin film due to mismatch between AlN and InAlN. Applying a layer of Al_2O_3 restricts the amount of relaxation along this free surface reintroducing a tensile stress that increases with increasing Al_2O_3 thickness. These trends in stress observed for both the planar and nanoribbon structures correlate well with the observed sheet resistance trends of the sample presented elsewhere[15] and plotted in Figure 3. Due to its piezo-electric nature, a tensile stress has been predicted to increase the concentration of electronic carriers in InAlN while a compression stress will cause a decrease in concentration. Therefore, based upon the trends in stress observed for the nanoribbon structure, it can be predicted that the electronic carrier concentration for an unpassivated nanoribbon device will be relatively low, resulting in a high sheet resistance, and will increase with increasing oxide thickness thus lowering the measured sheet resistance. However, the FEA model does not explain the dramatic decrease in sheet resistivity that is observed for large thicknesses of oxide (>45 nm). This sudden decrease in resistivity could be the result of the oxide layer coalescing creating an increased tensile stress in the InAlN layer in a manner similar to what has been observed for the coalescence of Volmer-Weber grown thin films.[20] Further investigations are underway to determine what affects device processing has on the stress in the HEMT layers and whether the coalescence of the Al_2O_3 film could generate stresses sufficient to cause the observed decrease in sheet resistance. The use of HOLZ line rocking curve simulations will also likely play an important role in producing more accurate elastic models as these methods have been shown useful in determining the shape of the displacement field in thin samples.[21]

In conclusion, we have demonstrated the combined use of CBED and FEA to investigate the stress state of both planar and nanoribbon-structured HEMT devices with nano-scale resolution. Kinematic simulations were used to measure amount of HOLZ line splitting in diffraction patterns obtained near the HEMT interface revealing a significant strain gradient along the [001] direction and generating profiles that could be compared to results from the FEA models, which suggest additional sources of stress not represented in our current models. Band plots and line scans of the ε_{xx}, ε_{yy}, and ε_{zz} strain components demonstrated the ability of the FEA model to correctly replicate the general splitting behavior observed experimentally. Finally, device structures were simulated to show the relationship between oxide layer thickness and stress state of the active InAlN HEMT layer which was then shown to be useful in explaining previously observed trends in sheet resistivity of the devices. Additionally, the techniques and methods used in this investigation can be applied to a much wider array of nanoscale materials in which stress and strain are traditionally challenging to characterize.
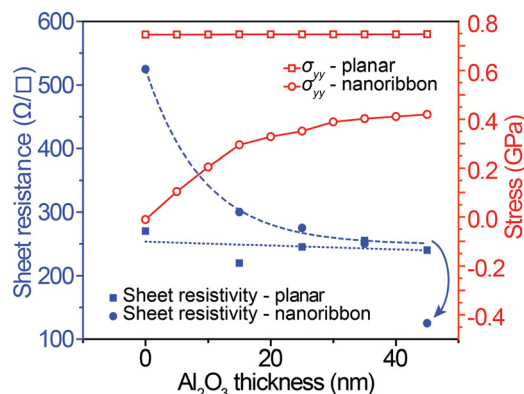
FIG. 3. The average stress (plotted in red) in the InAlN layer is calculated from FEA for device sized structures and is plotted as a function of the thickness of the passivating oxide layer for both planar and nanoribbon structures. Sheet resistance data (plotted in blue) from our previous investigation are replotted for comparison.[15] All lines are used as guides to the eye and emphasize the dramatic decrease in sheet resistance observed for the nanoribbon device at an Al_2O_3 thickness of 45 nm (indicated by arrow).

[1]T. Mårtensson, C. P. T. Svensson, B. A. Wacaser, M. W. Larsson, W. Seifert, K. Deppert, A. Gustafsson, L. R. Wallenberg, and L. Samuelson, Nano Lett. **4**, 1987 (2004).

[2]F. Qian, S. Gradečak, Y. Li, C. Y. Wen, and C. M. Lieber, Nano Lett. **5**, 2287 (2005); F. Qian, M. Brewster, S. K. Lim, Y. C. Ling, C. Greene, O. Laboutin, J. W. Johnson, S. Gradečak, Y. Cao, and Y. Li, Nano Lett. **12**, 3344 (2012).

[3]M. J. Tambe, S. K. Lim, M. J. Smith, L. F. Allard, and S. Gradečak, Appl. Phys. Lett. **93**, 151917 (2008).

[4]J. Xiang, W. Lu, Y. J. Hu, Y. Wu, H. Yan, and C. M. Lieber, Nature **441**, 489 (2006).

[5]N. Sköld, L. S. Karlsson, M. W. Larsson, M. E. Pistol, W. Seifert, J. Tragardh, and L. Samuelson, Nano Lett. **5**, 1943 (2005).

[6]D. Chrastina, G. M. Vanacore, M. Bollani, P. Boye, S. Schoder, M. Burghammer, R. Sordan, G. Isella, M. Zani, and A. Tagliaferri, Nanotechnology **23**, 155702 (2012).

[7]R. Balboni, S. Frabboni, and A. Armigliato, Philos. Mag. A **77**, 67 (1998); C. T. Chou, S. C. Anderson, D. J. H. Cockayne, A. Z. Sikorski, and M. R. Vaughan, Ultramicroscopy **55**, 334 (1994).

[8]F. Houdellier, C. Roucau, L. Clément, J. L. Rouviere, and M. J. Casanove, Ultramicroscopy **106**, 951 (2006).

[9]L. Clément, R. Pantel, L. F. Tz Kwakman, and J. L. Rouvière, Appl. Phys. Lett. **85**, 651 (2004).

[10]M. Fieger, M. Eickelkamp, L. R. Koshroo, Y. Dikme, A. Noculak, H. Kalisch, M. Heuken, R. H. Jansen, and A. Vescan, J. Cryst. Growth **298**, 843 (2007).

[11]Z. H. Feng, Y. G. Zhou, S. J. Cai, and K. M. Lau, Appl. Phys. Lett. **85**, 5248 (2004).

[12]J. Kuzmik, IEEE Electron Device Lett. **22**, 510 (2001).

[13]J. Kuzmik, A. Kostopoulos, G. Konstantinidis, J. F. Carlin, A. Georgakilas, and D. Pogany, IEEE Trans. Electron Devices **53**, 422 (2006).

[14]M. Azize and T. Palacios, Appl. Phys. Lett. **98**, 042103 (2011).

[15]M. Azize, A. L. Hsu, O. I. Saadat, M. Smith, X. Gao, S. P. Guo, S. Gradečak, and T. Palacios, IEEE Electron Device Lett. **32**, 1680 (2011).

[16]P. A. Stadelmann, Ultramicroscopy **21**, 131 (1987);

[17]M. Tanaka and K. Tsuda, J. Electron Microsc. **60**, S245 (2011).

[18]A. F. Wright, J. Appl. Phys. **82**, 2833 (1997).

[19]S. Christiansen, M. Albrecht, H. P. Strunk, and H. J. Maier, Appl. Phys. Lett. **64**, 3617 (1994).

[20]S. C. Seel, C. V. Thompson, S. J. Hearne, and J. A. Floro, J. Appl. Phys. **88**, 7079 (2000).

[21]L. Clément, F. Cacho, R. Pantel, and J. L. Rouviere, Micron **40**, 886 (2009); A. Spessot, S. Frabboni, R. Balboni, and A. Armigliato, J. Microsc. Oxford **226**, 140 (2007).